Tenth International Conference on Computational Fluid Dynamics (ICCFD10), Barcelona,Spain, July 9-13, 2018

ICCFD10-2018-xxxx

Large Eddy Simulation of a Finite Swept Wing undergoing Plunging Manoeuvre

C. Badoe[*,†], Z. Xie[*] and N. Sandham[*]
[†] Corresponding author:ceb1r14@soton.ac.uk

[*] AFM Research Group, University of Southampton, Southampton, SO17 1BJ, UK .

Simulations of the flow over a heaving NACA0012 finite wing are conducted to study the effect of sweep on the separated flow phenomena on the suction surface. An extensively-validated high-fidelity large-eddy simulation (LES) approach is used to examine the unsteady aerodynamic loads and flow structures at Reynolds number Re_c = 20,000 based on the chord. The simulations are carried out for reduced frequency k=0.94, a chord-normalized peak-to-peak amplitude of A/c=0.5, sweep angles $\Lambda = 0°$ and $\Lambda = 40°$ and angle of attack of 15°, representing post-stall conditions. Comparisons to experiment show good agreement in the time-averaged lift for $\Lambda = 0°$. The effect of sweep was found to result in a decrease in the time-averaged lift, maximum lift value as well as a delay in the dynamic stall process. A series of instantaneous spanwise vorticity plots show significant spanwise variations in the reverse flow region that develops over the suction surface during the start of the downstroke, giving rise to instabilities in the detached shear layer. For $\Lambda = 0°$ the LEV is highly three-dimensional near the tip region whereas it appears to be more two-dimensional for $\Lambda = 40°$. A comparison of the $\Lambda = 0°$ swept-wing with span-periodic (2D) computations show strong similarities of the dynamic stall vortex structure around the mid span region.

Keywords: Dynamic stall, Large-eddy simulations, Freestream turbulence, Swept wing, Transition

1 Introduction

Under oscillating conditions wings undergo “dynamic stall” phenomena, a behaviour that presents large hysteresis on the lift and moments when the time varying angle of incidence goes beyond its static stall angle, due to the unsteady wing motion [1-2]. The flow structure under these condition is characterised by the formation of both leading edge vortices (LEV) and trailing edge (TEV) vortices which creates a primary role in the lift enhancement. A wide range of experimental [3-8] and computational [9-14] studies have been conducted into the dynamic stall behaviour of oscillating wings from a two-dimensional (2D) perspective. These studies have provided insight into the flow instabilities at the leading edge during the oscillatory motion, including the formation and transition process. For example, our previous work [9] on the instabilities of the (LEV) structure of a heaving wing showed that the LEV system experiences perturbations across the span, breaking down into small scale structures within its core. A potential mechanism for the breakdown was found to be the presence of an elliptic instability of the vortex core, initiated by contact with the reverse flow vortex. The detachment of the LEV was also found to result in a decrease in lift and an increase in pitching moment.

The aerodynamic load and flow structure developing over a finite-span wing which is the subject of the present contribution, has received much less attention than its two-dimensional counterpart partly due to the large computational cost involved to capture the flow details and the limited experimental data. Wings of finite span exhibit a complex three-dimensional flow structure, in particular near the wing tip which interacts with the spanwise vortical structures generated by the oscillatory motion. In an effort to understand the flow structure in such conditions, [15] first studied the dynamic stall phenomena of a NACA-0015 wing with finite span using a Reynolds-averaged Navier-Stokes (RANS) methodology. The unsteady flowfield was compared with experiments from [16]. The study was limited to a coarse grid resolution. Since then, others such as

[17-21] have also used RANS methods with improved resolution for such complex unsteady three-dimensional (3D) simulations. In all these studies, the RANS methodology was found to be insufficient to predict such a time-dependent flow structure. With advances in computing power, high fidelity approaches such as large-eddy simulation (LES) and direct numerical simulations (DNS) are now being used to capture the details of such flow.

The aerodynamic loads and flow structure of a low-aspect-ratio finite wing under plunging conditions were studied by [22] using an LES approach. Results were presented for a mean angle of attack of 8°, Reynolds number $Re_c = 10^4$, reduced frequency $k = 1.0$ and amplitude $h/c = 0.25$. The computed results were found to be in good agreement with experimental results. Their results also showed that the LEV evolves into an arch-type structure whose leg moves towards the wings centreline and reconnects to form a ring-like structure which is shed as the next plunging cycle begins. The evolution and breakdown of the wing tip vortex structure was also observed in the computations. The effect of upstream disturbances in the flow was not considered in their computations. Others, such as [23-25], have also examined the vortex structure and wake topologies of finite wings using LES or DNS methodologies.

Most of the limited research on the dynamic stall of oscillating finite wings have been directed towards the un-swept configuration, whilst the effect of sweep on the behaviour of the LEV dynamics have received little attention. Experimental investigations by [26-28] concentrated on the aerodynamic loads and mean flow properties of swept wing configurations. More recently [29] performed DNS including the transition to turbulence of separation bubbles over a NACA0012 swept wing and showed that the effect of sweep leads to an increase of the separation bubble on the suction side of the wing and a delay of the laminar-to-turbulent transition process. The work of [29] was carried out for a fixed wing at a $Re_c = 5 \times 10^4$.

The effect of upstream disturbances over a swept wing configuration has been studied by [30]. The authors investigated the role of two different sets of freestream turbulence characteristics over a fixed swept wing using DNS and showed that increasing the turbulent intensity by one order whilst keeping the same integral length scale produced a linear behaviour in terms of transition location.

Kaltenbach and Janke [31] conducted a DNS study of flow separation behind a swept, rearwards-facing step and showed that the instability growth rate at the detached shear layer grow slightly with sweep angle.

The vortex structure of a pitching swept wing was studied by [32]. Their results showed that, compared to stationary wing, the vortex breakdown location of a swept configuration has a large phase difference with the wing motion and a time delay exists in the flow structure of the pitching motion as compared to the stationary flow field.

In this work, the physics behind the unsteady aerodynamics of a plunging finite swept wing is presented. Aerodynamic loads and the wing tip vortex effect are assessed by comparing the results to an un-swept case. An analysis of the flow instabilities at the leading edge and the role of these instabilities in the transition of the separation bubble is also presented. The effect of the wing tip vortex is also assessed by comparing the results with a previously computed span-periodic condition.

2 Numerical Methodology

2.1 Large eddy simulations

Large eddy simulations are carried out using the open-source finite volume solver OpenFOAM version 2.3.0. Within the assumption of an incompressible fluid and by denoting the filtering operation with an overbar, the set of equations may be written in the form:

$$\frac{\partial \overline{u}_i}{\partial x_i} = 0 \tag{1}$$

$$\frac{\partial \overline{u}_i}{\partial t} + \frac{\partial \overline{u}_i \overline{u}_j}{\partial x_j} = -\frac{1}{\rho}\frac{\partial \overline{p}}{\partial x_i} + \frac{\partial}{\partial x_j}\left(\nu \frac{\partial \overline{u}_i}{\partial x_j} - \tau_{ij}^r\right), \tag{2}$$

where τ_{ij}^r is the non-linear subgrid-scale (SGS) stress tensor which should be modeled. Thus,

$$\tau_{ij}^r = \overline{u_i u_j} - \overline{u}_i \overline{u}_j \tag{3}$$

$$\tau_{ij}^r = -2\nu_t \overline{S}_{ij} + \frac{1}{3}\delta_{ij}\tau_{kk}, \tag{4}$$

where the Kronecker delta $\delta_{ij} = 1$ for $i = j$, otherwise $\delta_{ij} = 0$; ν_t is the SGS eddy viscosity and $\overline{S}_{ij}$ is the rate-of-strain tensor for the resolved scale defined by

$$\overline{S}_{ij} = \frac{1}{2}\left(\frac{\partial \overline{u}_i}{\partial x_j} + \frac{\partial \overline{u}_j}{\partial x_i}\right). \tag{5}$$

The mixed time-scale (MTS) model of [33] has been used. The advantages of this models is that the eddy viscosity goes naturally to zero in the wall region, so neither constant adjustments nor damping functions are needed to compute wall bounded flows. The model has also been credible when applied to transitional flow past oscillating wings [9,34] at comparable Reynolds number.

2.2 Simulation parameters and flow configuration

Large eddy simulations have been performed for the flow over a finite swept wing configuration. The wing section has a NACA 0012 profile with chord $c = 0.0627$m, aspect ratio $AR = 5$ mounted with a $2c$ gap between the tip and side wall. The wing was modified to include a sharp trailing edge. Unsteady and phase-averaged computations were conducted with a sinusoidal plunging motion $y = A\sin(2\pi ft)$ (see Figure 1), reduced frequency k =0.94, peak-to-peak amplitude $A/c = 0.5$ and angle of attack $\alpha = 15^\circ$ representative of post-stall conditions. The investigation is carried out for sweep angle $\Lambda = 40^\circ$ and an un-swept wing case $\Lambda = 0^\circ$ is included for comparison purpose. The streamwise section of the wing is a NACA 0012 profile of similar chord length (see Figure 2a). The Reynolds number based on the airfoil chord is $Re_c = 2 \times 10^4$.

The computational domain was created using Pointwise version 16. A C-type grid was adopted close to the wing surface. Away from the wing surface, an H-type grid was used. Grid points were concentrated around the wing boundary layer to capture the transition process. The domain was extruded in the spanwise direction by $7c$ and had a spacing of about 840 to 1100 cells, aiming to provide $5 \leq \triangle z^+ \leq 10$ over the wing surface. The majority of the cells were clustered around the tip region to capture the tip vortices. The maximum and minimum spacing was $(\Delta z/c)_{max} = 6.0\times10^{-3}$ and $(\Delta z/c)_{min} = 3.0\times10^{-3}$ at the root and tip respectively. For the wall normal spacing, the mesh was designed to satisfy a $y^+ \leq 1$ criterion at the wall. An approximate $\triangle x^+ \leq 10$ was also achieved on the wing surface. In the near wake region (from the wing trailing edge to a distance of 4 chords) the spacing was kept uniform and a cell aspect ratio of 1 was maintained to capture the anticipated near wake vortices.

Boundary conditions include no-slip and symmetry conditions at the wall and the two lateral boundaries respectively. Heaving computations were started from a previously simulated static condition (static cases were computed for about 10 chord flow pasts) and then run for about 7 cycles. Data was processed from the third cycle onwards.

A second order implicit scheme was used for the temporal discretization and the bounded second order (Gamma) scheme, with a factor $\Gamma = 0.25$ [35] was used for the convection term. The time step $\triangle t U_\infty/c = 8.0 \times 10^{-4}$ corresponds to 4000 time steps per cycle. The pimpleDyMFoam solver in OpenFOAM was used, which is a transient solver for incompressible flow on a moving mesh utilising the PIMPLE (merged PISO-SIMPLE) agorithm. The PIMPLE algorithm includes both under-relaxation and velocity correction and is mainly used for transient flows, but without the same Courant number constraints of the PISO algorithm. The number of outer iterations was set to two and the number of pressure corrections was set to three.

Due to the computational resources involved when using LES computations in combinations with large aspect ratio wings, grid sensitivity analysis was performed for a span-periodic (2D) case using a span width of $0.25c$ and sweep angle $\Lambda = 0^\circ$. The grid and span width size was chosen based on previous study [9] of the wing configuration analysed in this work. A summary of the features of the grid system employed is shown in Table 1, where the computational domain size is normalised by the wing chord c and L_U, L_H, L_W and L_Z are the upstream length, domain height, wake length and span length respectively. N_{AU} is the number of grid points on the wing upper surface, N_{AL} is the number of grid points on the wing lower surface and $\Delta z/c$ is the spanwise spacing. Based on the grid dependency studies, grid G2, representing a reasonable compromise in accuracy and computational cost, was used to construct the final three-dimensional grid which extended a distance of s=7.0c. Hence the grid size for the three-dimensional grid was 645×249×1100. An illustration of the grid generated on the finite-wing and gap region is shown in Figure 2b and Figure 2c respectively.

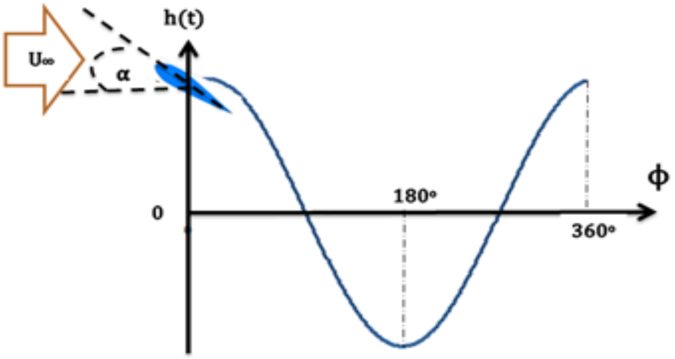

Figure 1: Illustration of heaving motion, where denoting phase angle $0° \leq \phi \leq 360°$.

Table 1: Grid and domain parameters, $Re_c = 2 \times 10^4$, $\alpha = 15°$, $k = 0.94$ and $A/c = 0.5$

$Mesh$	$Size$	N_{AU}	N_{AL}	$\Delta z/c$	$L_U[c]$	$L_W[c]$	$L_H[c]$	$L_Z[c]$
G1	456×176×30	176	176	0.0083	7.0	14.4	4.05	0.25
G2	645×249×43	249	249	0.0058	7.0	14.4	4.05	0.25
G3	912×352×60	352	352	0.0041	7.0	14.4	4.05	0.25

3 Results

3.1 Aerodynamic loads

Figures 4(a) show the phased-averaged lift as a function of the effective angle of attack and 4b shows the time-averaged lift as a function of the heaving reduced frequency respectively for the swept and un-swept wing configuration. The un-swept results are compared with measurements by [36] who carried out similar analysis for a range of reduced frequencies from $k = 0.47$ to $k = 0.94$. The lift coefficient of a span-periodic case [9] has also been included for comparison purpose. Note that the lift coefficient in the computations are integrated over the wing surface and the hysteresis loop was obtained by averaging over three cycles. The span-periodic (2D) case show strong fluctuations as the wing approaches stall. The lift slope and maximum lift value are higher compared to the un-swept finite wing. This may be due to the fact that the presence of the wing tip vortices weakens the dynamic stall vortex structure across the span in the un-swept finite wing computation, thus influencing the overall lift. Although not shown here, there is also a shift in the pitching moment, specifically the maximum C_m between the span-periodic and un-swept finite wing cases. The time averaged lift at $k = 0.94$ for the un-swept finite wing agrees closely with the experiment by [36]. Compared to the span-periodic case, a reduction in lift of about 25% is observed, which may be attributed to the deformation of the inwards LEV from the wing tip.

The effect of sweep is evident in Figure 4a. The hysteresis loop is much narrower compared to the un-swept configuration. Note that to provide a standard comparison, the computations in Figure 4a were based on the velocity components normal to the leading edge which relates to the inflow by $Q_\infty = U_\infty$ cos Λ, hence $Q_\infty = 1.0$ for both swept and un-swept cases. Sweep appears to delay the onset of dynamic stall and reduces the maximum lift value. The maximum lift value for the swept wing occur at α_{eff}= 40°. After stall the lift values of the swept wing are also lower than the un-swept wing. Prominent elements of the

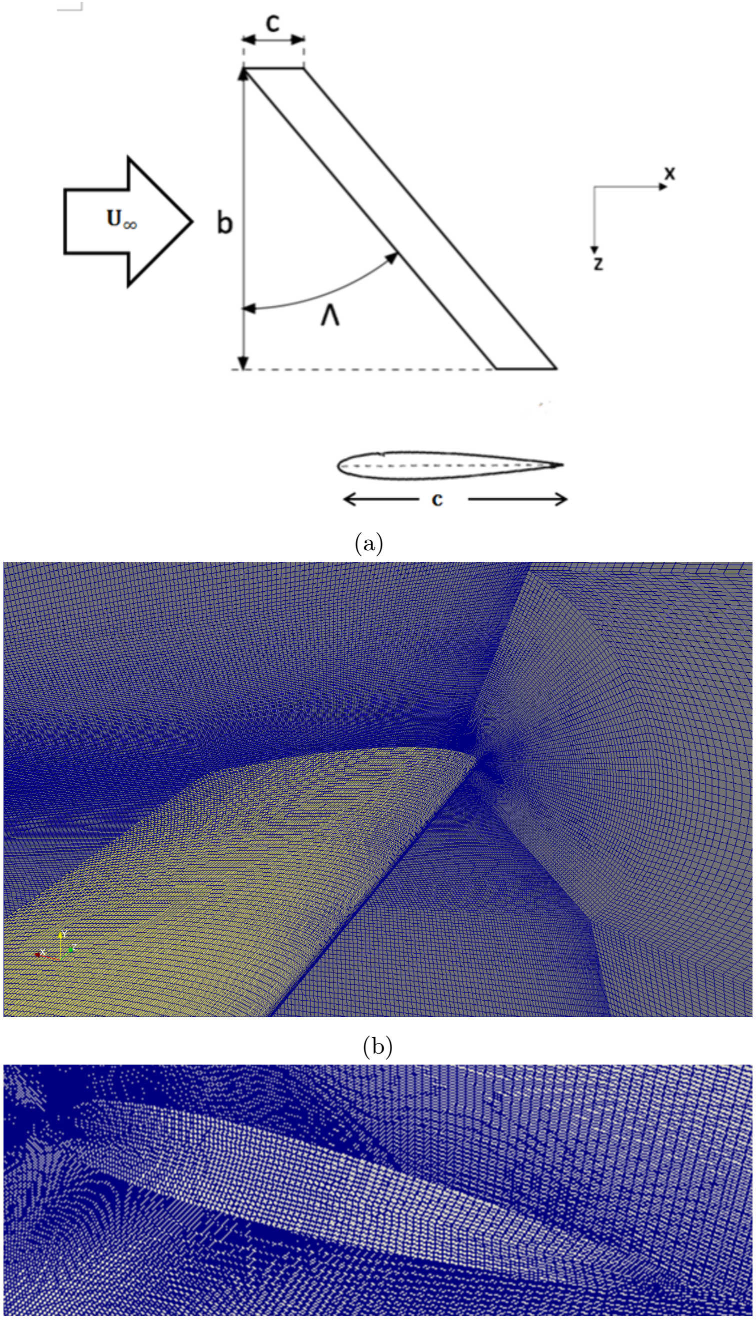

(a)

(b)

(c)

Figure 2: (a) Sketch of the swept-wing configuration where U_∞, c, $\wedge$ denotes freestream velocity, wing chord and sweep angle respectively. Sweep is defined as the angle between the leading edge and spanwise axis (b) Details of the mesh around the wing and (c) gap region.

flow in this region are the separated shear layer emanating from the leading edge and the development of the trailing edge vortices. It is interesting to note that the mean lift value for the un-swept wing agrees closely with experimental values of [36], despite the fact that the computations did not take into account inflow disturbances and end wall effects as they usually exist in experiments. According to [37] meaningful comparison is possible depending on the motion parameters that determine the LEV development.

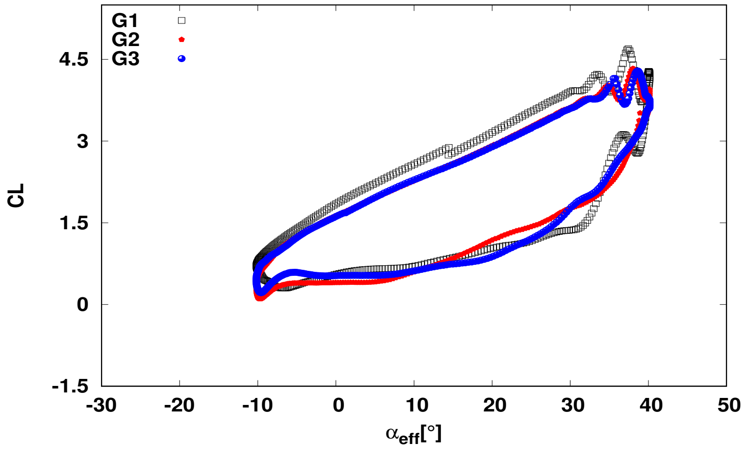

Figure 3: The effect of grid resolution on the computed lift coefficient, $\alpha = 15°$, $Re_c = 2 \times 10^4$, $k = 0.94$ and $A/c = 0.5$.

3.2 Phase-averaged flow features

A view of the flow features is provided in Figures 6-8 showing the phase-averaged distribution of spanwise vorticity at selected phases of the heaving cycle. The plots are taken at six spanwise locations from the tip $z/b = 0$ to the root $z/b = 1$ of the wing as shown in Figure 5. At $\phi = 0°$, the wing is at its maximum displacement and an attached flow is observed. The flow structure is similar for both swept and un-swept configurations. No roll-up of the leading edge vortex can be seen at this phase of the plunging cycle. The flow is also similar across the span, with the trailing edge separation and near-wake vortical structures that were shed from the previous cycle visible.

As the wing continues to move downwards from $\phi = 0°$ to $\phi = 90°$ it undergoes dynamic stall which is characterised by the formation of the LEV system. A key prominent feature is the development of the wing tip vortex as a result of the gap region. The wing tip vortex appears to be much stronger at $z/b = 0.05$ and $z/b = 0.15$, (see also the skin friction plot in Figure 10a) in the un-swept wing configuration. Notice that while reattachment of the flow is observed at mid-span ($z/b = 0.5$) for the swept wing, the flow never reattaches to the surface of the un-swept wing. This is also seen in the skin friction plot in Figure 10b. The skin friction plot also shows some turbulent patches in the reattachment region, specifically at x/c=0.35 for the swept wing.

As the wing continues to decelerate at $\phi = 180°$, it reaches its lowest displacement during the heaving cycle. The main LEV has been shed downstream in all cases. The secondary vortices at the leading edge ($z/b = 0.15$ and $z/b = 0.25$) are more prominent in the un-swept configuration. Skin friction plots in Fig 11a show evidence of perturbations from the leading edge up until $0.1c$ for both cases. The flow then becomes laminar downstream after in the swept wing configuration. However, in the un-swept case, perturbations can be seen at $0.3c$. At midspan ($z/b = 0.5$) the reverse flow is much stronger for the swept case and appears to have broken down the secondary vortices into smaller discrete vortices. The location and size of the main LEV across the span differs for both configurations (see Figure 11b). The magnitude of the pressure coefficient (see figure 12) at this phase of the cycle decreases with sweep angle contributing to the the differences in mean-lift observed in the plot in Figure 4a.

Comparing the un-swept finite wing to a span-periodic case in Figure 9, the mid-span is first considered. From an attached boundary layer when the wing is at its maximum displacement, the main LEV is initiated as the wing travels on its downstroke. Lift and moments change rapidly. In contrast to the span-periodic condition, the size and intensity of the main LEV differs and there appears to be no coherence of the structures across the span. The tip vortices suppress the separation, preventing the development of the LEV for about 10-15% of the span length. The effect of this phenomenon is a reduction in mean lift and a downwards shift in the lift hysteresis compared to the span-periodic condition. This behaviour has also been reported by [22,36,38].

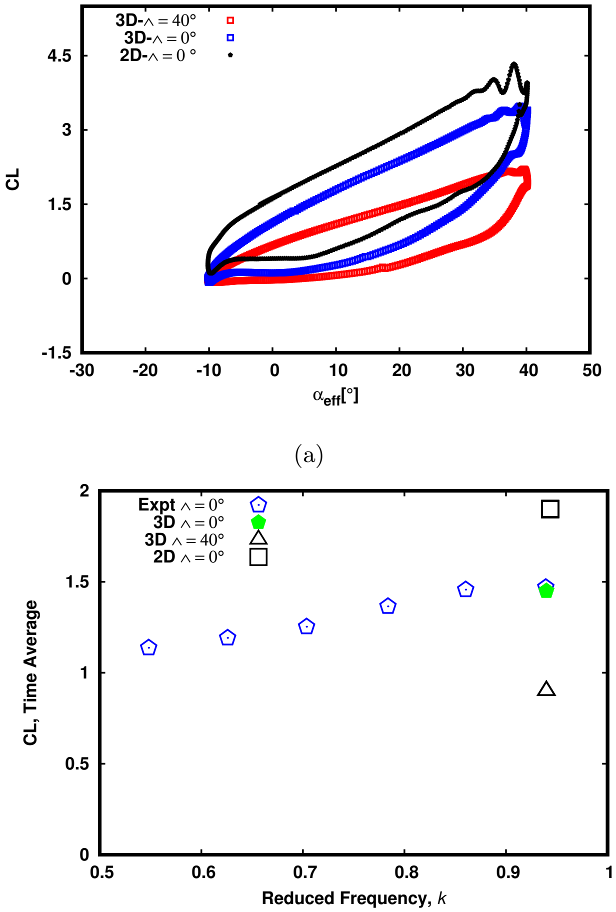

(a)

(b)

Figure 4: Phase-averaged lift coefficient as a function of heave-induced effective angle of attack (a) and time-averaged lift as a function of the heaving reduced frequency, k (b), $\alpha = 15°$, $Re_c = 2 \times 10^4$, $k = 0.94$ and $A/c = 0.5$; Experimental results from [36].

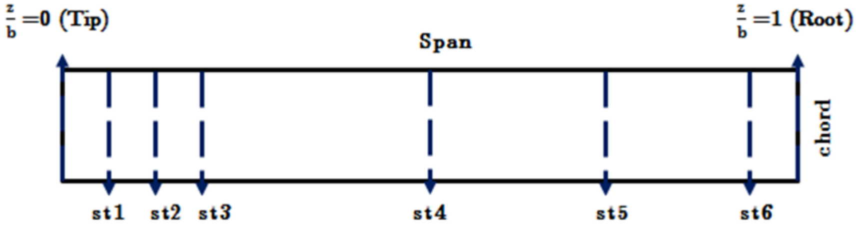

Figure 5: Spanwise cuts, where z/b=0 corresponds to the tip and z/b=1 is the root ($st1$:z/b=0.05, $st2$:z/b = 0.15, $st3$:z/b=0.25, $st4$:z/b=0.5, $st5$:z/b=0.75, $st6$:z/b=0.95).

3.3 Unsteady flow features

Figures 12 and 13 show the instantaneous flow structures over the suction surface of the wing through the iso-surfaces of the second invariant of the velocity gradient tensor (Q-criterion) over four phases of the heaving cycle for both swept and un-swept wing configurations. The tip vortex is visible in all snapshots. When the wing is at its maximum displacement at $\phi = 0°$, the flow is attached at the leading edge and across the span. In both cases the tip vortex, in comparison to the other phases of the cycle, is relatively small. It is

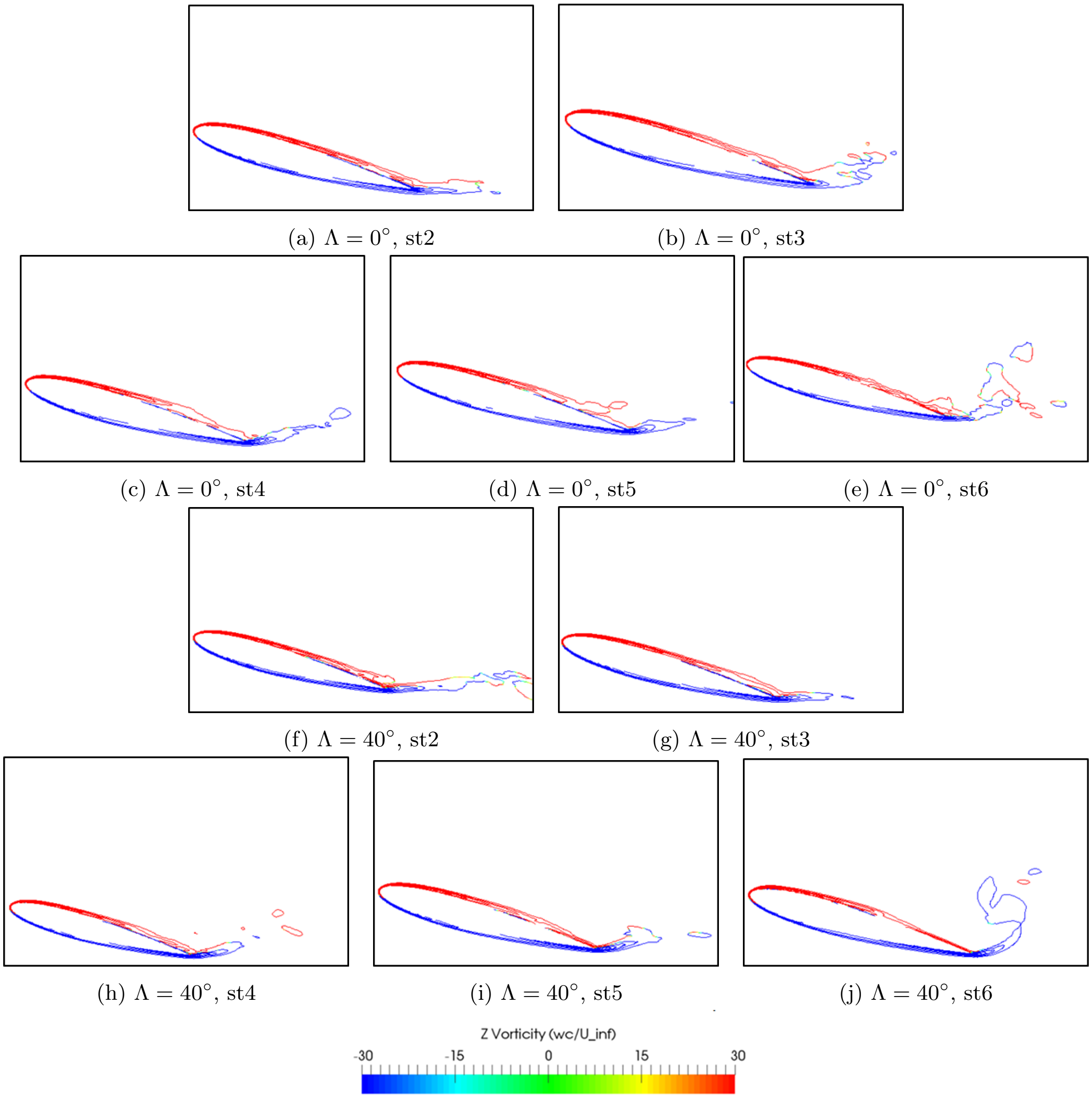

(a) $\Lambda = 0°$, st2

(b) $\Lambda = 0°$, st3

(c) $\Lambda = 0°$, st4

(d) $\Lambda = 0°$, st5

(e) $\Lambda = 0°$, st6

(f) $\Lambda = 40°$, st2

(g) $\Lambda = 40°$, st3

(h) $\Lambda = 40°$, st4

(i) $\Lambda = 40°$, st5

(j) $\Lambda = 40°$, st6

Figure 6: Phase-averaged contour plot of spanwise vorticity for $\phi = 0°$, $\alpha = 15°$, $k = 0.94$ and $A/c = 0.5$.

interesting to note the presence of the shed vortices from the previous cycle at the trailing edge, especially the counter-clockwise vortices are more evident in the un-swept wing configuration, whilst it appears to have broken down in the swept case. Compared to the swept wing, the trailing edge structures seem to be unsteady. This is seen more clearly in the instantaneous vorticity plots in Figure 14.

As the wing travels on its downstroke at $\phi = 90°$ the leading edge vortex is formed and appears to be three-dimensional in nature in the un-swept case across the span and of similar wavelength (with the exception of small regions around the tip). The dynamic stall vortex structure for the un-swept wing at mid-span exhibit similar characteristics to that observed by [9] for a span-periodic configuration (see also Figure 9). The influence of sweep results in a weaker LEV structure, which appears to be two-dimensional in nature. The tip vortex is well defined in both wings compared to the previous cycle. By the time the wing reaches its minimum point in the cycle ($\phi = 180°$), the flow becomes highly three-dimensional in both wing configurations. The main LEV has evolved into several arch-type structures. The arch-type structures are then shed as ring-shaped structures downstream and into the wake. The arch-like structures across the

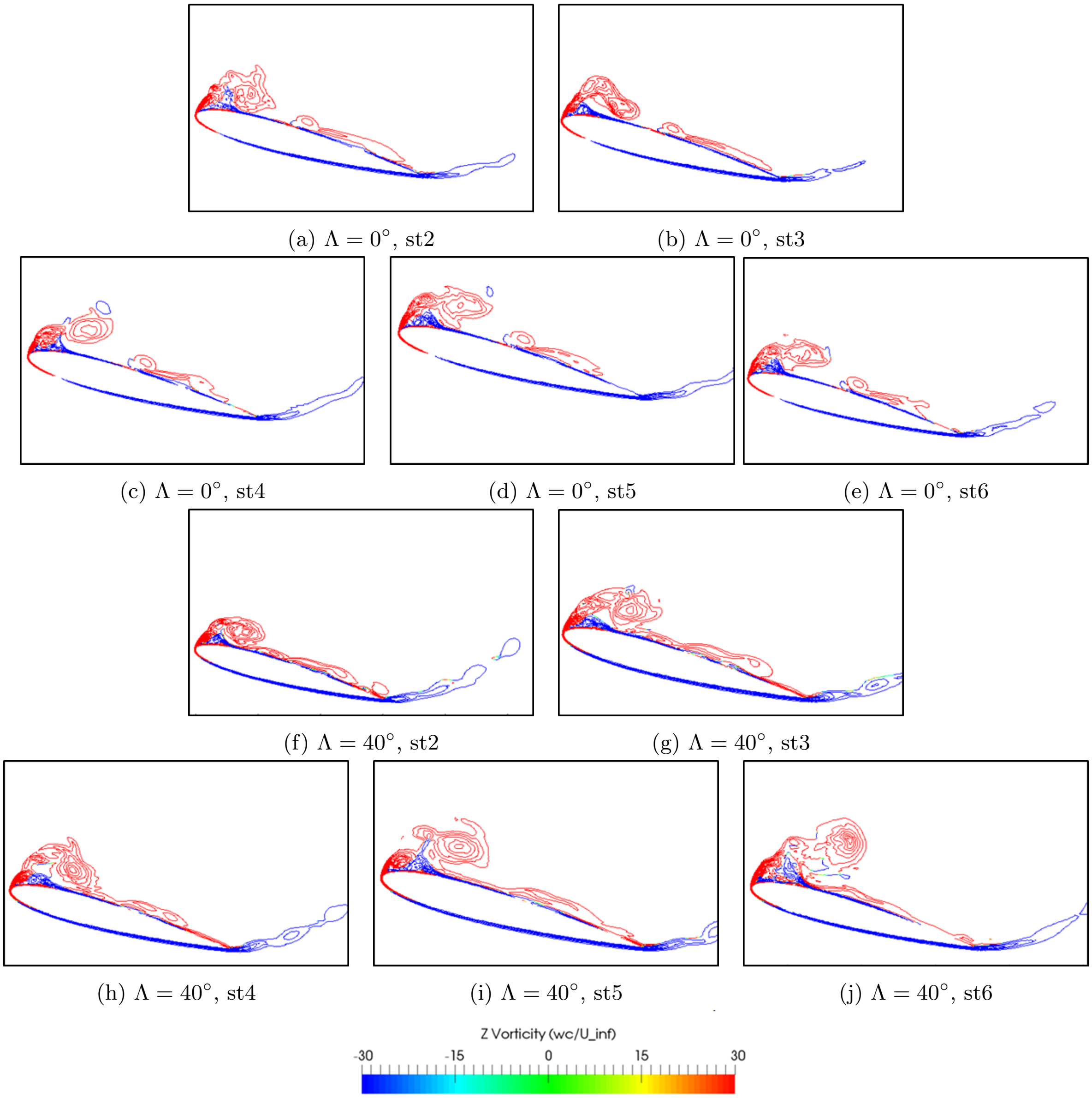
(a) $\Lambda = 0°$, st2

(b) $\Lambda = 0°$, st3

(c) $\Lambda = 0°$, st4

(d) $\Lambda = 0°$, st5

(e) $\Lambda = 0°$, st6

(f) $\Lambda = 40°$, st2

(g) $\Lambda = 40°$, st3

(h) $\Lambda = 40°$, st4

(i) $\Lambda = 40°$, st5

(j) $\Lambda = 40°$, st6

Figure 7: Phase-averaged contour plot of spanwise vorticity for $\phi = 90°$, $\alpha = 15°$, $k = 0.94$ and $A/c = 0.5$.

wing span are larger in the un-swept case. The reverse flow is highly three-dimensional compared to the swept case and covers a large portion around the tip region. As the wing embarks on its upstroke at $\phi = 270°$ all the arch-type structures in the un-swept case have been transformed into ring-shaped structures as they are shed from the wing. However in the swept case some arch-shaped structures are still visible, specifically at x=0.4c and there appears to be a delay in the detachment of the arch-shaped structures from the wing surface (see also Figure 14). The evolution and detachment of the arch-shaped vortex structures for a plunging finite wing under similar conditions was also observed by [22,36].

Instabilities around the core of the LEV structure was observed for both wing configurations during the downstroke. In order to understand the underlying mechanisms, contours of spanwise vorticity (w_z), plotted for $(x - z)$ planes through the various vortex structures, are evaluated for the swept and un-swept wing configurations. The plots are carried out at $\phi = 70°$ as shown in Figure 15(top), where points A and B are clockwise vortices and C is the recirculating region where the vortices are anti-clockwise in nature. Figure 15(bottom) shows the location of $(x - z)$ planes through the structures A to C.

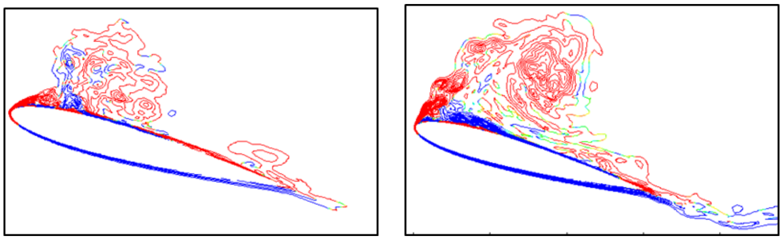

(a) $\Lambda = 0°$, st2 (b) $\Lambda = 0°$, st3

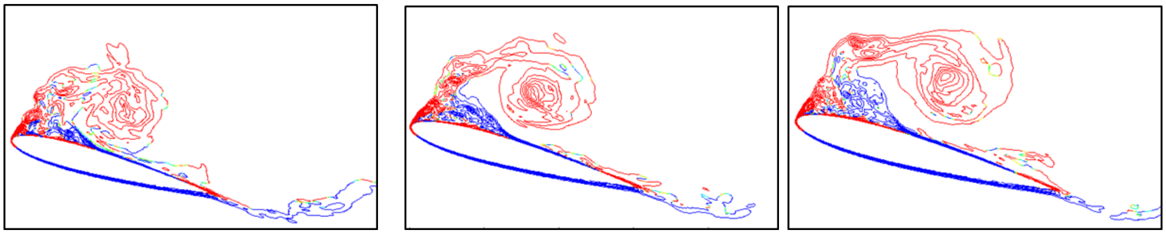

(c) $\Lambda = 0°$, st4 (d) $\Lambda = 0°$, st5 (e) $\Lambda = 0°$, st6

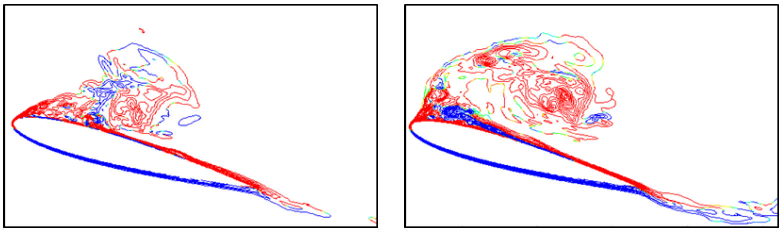

(f) $\Lambda = 40°$, st2 (g) $\Lambda = 40°$, st3

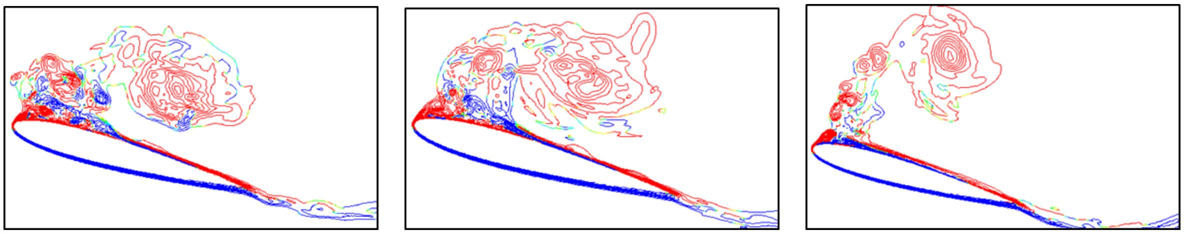

(h) $\Lambda = 40°$, st4 (i) $\Lambda = 40°$, st5 (j) $\Lambda = 40°$, st6

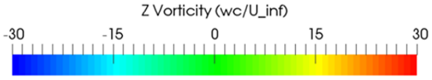

Figure 8: Phase-averaged contour plot of spanwise vorticity for $\phi = 180°$, $\alpha = 15°$, $k = 0.94$ and $A/c = 0.5$.

Starting with $\Lambda = 0°(L1)$ in figure 16, the tip region is highly three-dimensional and the perturbations inside the cores A and B are of non-uniform amplitude across the span compared to $\Lambda = 40°(L1)$ and $\Lambda = 40°(L2)$. Closer to the tip region a small region of reverse flow (also three-dimensional in nature) can be observed within $\Lambda = 0°(L1)$. This reverse flow region seems to have broken down within the core of A in $\Lambda = 40°(L1)$. Close to the mid-span region w_z structures appear to be two-dimensional in the swept configuration (see $\Lambda = 40°(L1)$ and $\Lambda = 40°(L2)$). Two recirculation regions can be seen in the swept case, a primary region underneath the shear layer and secondary region underneath the secondary LEV, whilst in the un-swept configuration only one region is visible. The core of the secondary recirculation region for the swept case is two-dimensional compared to the primary region at $\Lambda = 40°(L3)$. The core of C in $\Lambda = 0°(L2)$, which is also three-dimensional in nature, causes instabilities in the detached shear layer which is starting to roll up. Three-dimensional flow structures can be seen close to the tip region in the un-swept configuration within the core of C at $\Lambda = 0°(L2)$ whereas in $\Lambda = 40°(L3)$, the w_z structures are two-dimensional in nature. This is also seen more clearly in the plots in Figure 14 at $\phi = 90°$. The instability mechanism around the

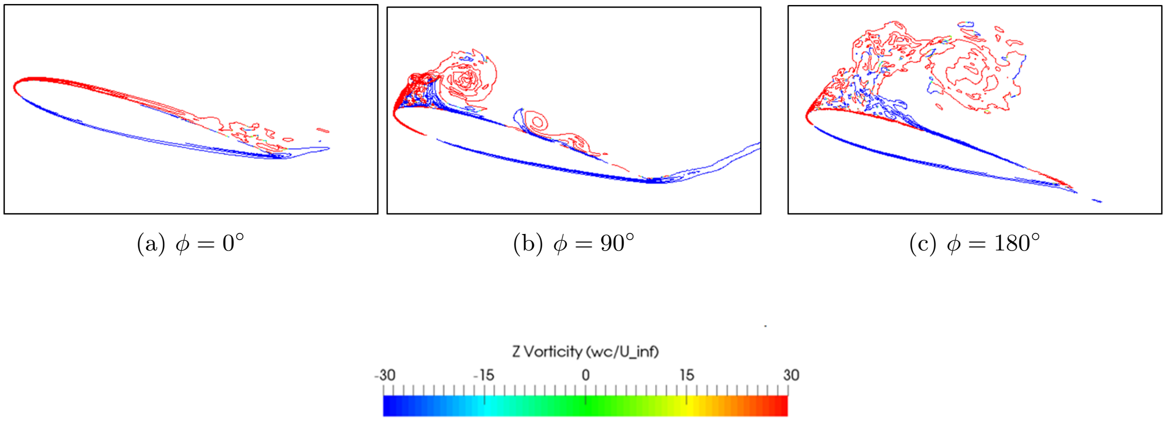

(a) $\phi = 0°$ (b) $\phi = 90°$ (c) $\phi = 180°$

Figure 9: Phase-averaged contour plot of spanwise vorticity, for span-periodic case [9], $Re_c = 2 \times 10^4$, $\alpha = 15^0$, $k = 0.94$ and $A/c = 0.5$.

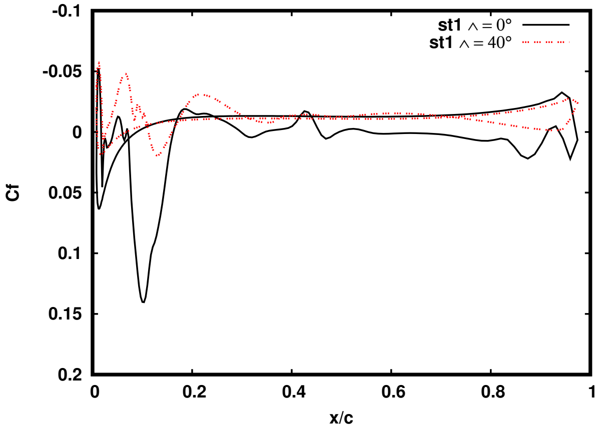

(a) $z/b = 0.05, st1$

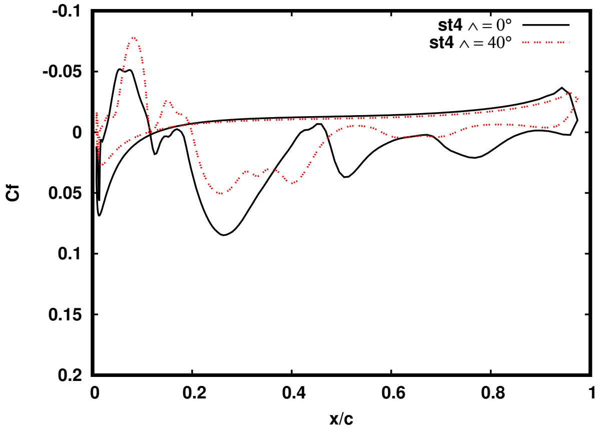

(b) $z/b = 0.5, st4$

Figure 10: Skin friction coefficients at $\phi = 90°$, $\alpha = 15°$, $Re_c = 2 \times 10^4$, $k = 0.94$ and $A/c = 0.5$.

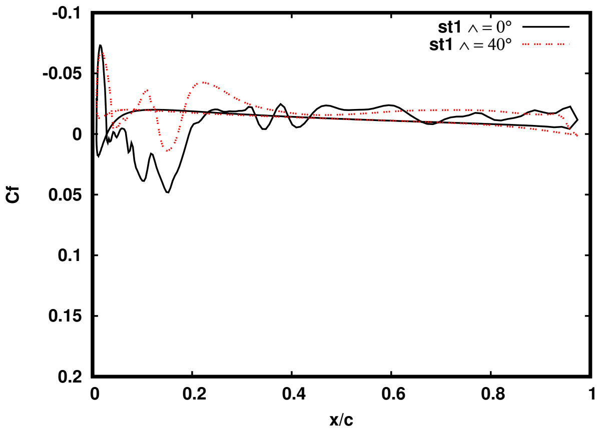

(a) $z/b = 0.05, st1$

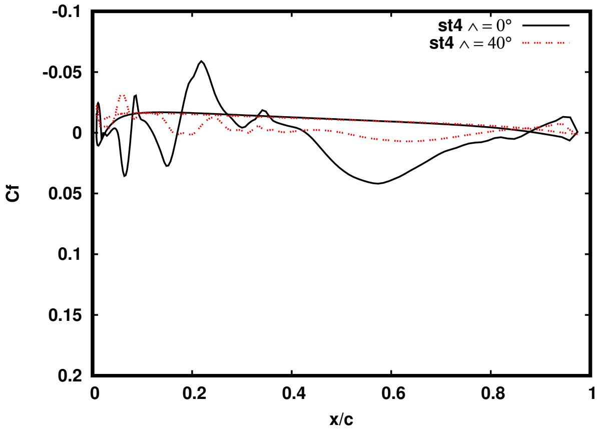

(b) $z/b = 0.5, st4$

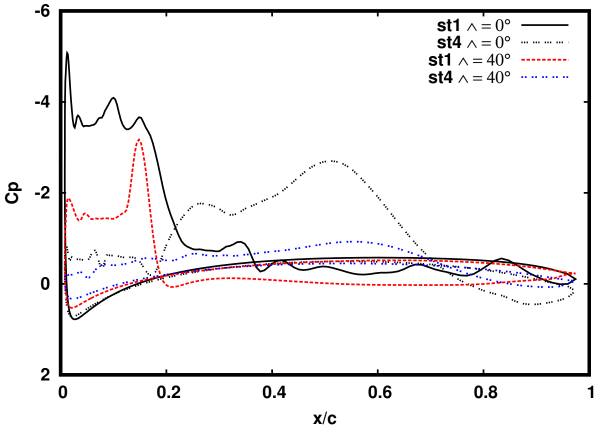

(c) $z/b = 0.05, st1$ and $z/b = 0.5, st4$

Figure 11: Skin friction coefficients (a,b) and pressure coefficient (c) at $\phi = 180°$, $\alpha = 15°$, $Re_c = 2 \times 10^4$, $k = 0.94$ and $A/c = 0.5$.

mid-span region in the un-swept configuration shows strong similarities to that of a span-periodic wing investigated by [9].

4 Conclusion and Future Work

An advanced LES approach has been used to gain valuable insight into the effect of finite span and sweep angle on the dynamic stall phenomena, more especially the LEV formation and breakdown. Computational results for the high-aspect-ratio un-swept wing was also compared with previous span-periodic heaving wing computations. For the un-swept finite wing, the presence of the wing tip vortices weakens the dynamic stall vortex structure across the span, hence reducing the mean and maximum lift values compared to the span-periodic wing. However the spanwise vortical structures of the span-periodic wing were found to be comparable to the un-swept wing in the mid-span region.

Dynamic stall phenomena for the un-swept wing is characterised by the formation of the leading edge vortex which evolves into an arch-type structure and then shed as ring-like structures during the start of the next heaving cycle. The effect of sweep resulted in a significant decrease in the lift slope as well as the maximum lift value and a delay in the dynamic stall process.

Analysis of the instantaneous flow structures at $\phi = 70^\circ$ within the core of the dynamic stall vortex showed three-dimensional disturbances close to the tip region in the un-swept configuration, whereas the swept case remained two-dimensional around the tip region. In all configurations, transition to turbulence was observed in the LEV and disturbances were observed down to the wing surface. The transition to turbulence and the LEV shedding process are similar to those reported in [36] at a similar Reynolds number.

Future work should focus on external disturbances, wall conditions effects as well as investigating the instabilities at the leading and trailing edge in combination with a pitching motion.

Acknowledgements

This work was supported by Engineering and Physical Sciences Research Council (EPSRC) grant EP/M022692/1. The authors acknowledge the use of IRIDIS High Perfomance Computing Facility at the University of Southampton and the UK National Supercomputing Service Archer supported by the EPSRC under grant EP/L000261/1.

References

[1] McAlister, W., Carr, L.W. and McCroskey, W.J. Analysis of the development of dynamic stall based on oscillating airfoil experiment. *Tech. Rep. NASA Tech. Mem.*8382 (1977).

[2] McCroskey, W.J. The phenomenon of dynamic stall. *Tech. Rep. TR 81-A-6. NASA.* (1981).

[3] Leishman, J. Dynamic stall experiments on the NACA 23012 aerofoil. *J. Expt Fluids.* (1990) **9**:49–58.

[4] Lee, T. and Gerontakos, P. Investigation of flow over over an oscillating airfoil. *J. Fluid Mech.* (2004) **512**:313–341.

[5] Rudmin, D., Benaissa, A. and Poirel, D. Detection of laminar flow separation and transition on a NACA 0012 airfoil using surface hot-films. *J. Fluids Eng.* (2013) **135**:101104–1.

[6] Kim, D.H. and Chang, J.W. Low-Reynolds-number effect on the aerodynamic characteristics of a pitching NACA0012 airfoil. *J. Aero Sci Tech.* (2014) **32**:162–168.

[7] Cleaver, D.J., Gursul, I., Wang, Z. and Calderon, D.E. Lift enhancement through flexibility of plunging wings at low Reynolds numbers. *J. Fluids Struct.* (2016) **64**:27–45.

[8] Chiereghin, N., Gursul, I. and Cleaver, D.J. Unsteady Measurements for a periodically plunging airfoil. *AIAA Paper.* (2017) **7**:2017-0996.

[9] Badoe, C.E., Zheng-Tong, X. and Sandham, N.D. Performance analysis of a plunging wing at low Reynolds number. *ECCM 6-ECFD 7.* (2018) .

[10] Medjroubi, W., Stoevesandt, B., Carmo, B. and Peinke, J. High-order numerical simulations of the flow around a heaving wing. *Compt Fluids.* (2011) **51**:68–84.

[11] Peinke, J., Stoevesandt, B. and Medjroubi, W. Wake classification of heaving airfoils using spectral/hp element method. *J. Compt Appl Maths.* (2012) **236**:3774–3782.

[12] Barakos, G.N. and Drikakis, D. Unsteady separated flows over maneuvering lifting surfaces. *Philos. Trans R Soc Lond.* (2000) **358**:3279–91.

[13] Wang, S., Ingham, D.B., Ma, L., Pourkashanian, M. and Tao, Z. Numerical investigations on dynamic stall of low Reynolds number flow around oscillating airfoils. *Compt Fluids.* (2010) **39**:1529–1541.

[14] Wang, L., Li, L. and Fu, S. A comparative study of DES type methods for mild flow separation prediction on a NACA0015 airfoil. *Int J. Num Mthds for Heat and Fluid Flows.* (2017) **27**:2528–2543.

[15] Ekaterinaris, J.A. Numerical investigation of dynamic stall of an oscillating wing. *AIAA Journal.* (1995) **33**:1803–1808.

[16] Piziali, R. 2-D and 3-D oscillating wing aerodynamics for a range of angle of attack including stall. *NASA TM 4632.* (1994) .

[17] Wang, S., Ingham, D.B., Ma, L., Pourkashanian, M. and Tao, Z. Turbulence modeling of deep dynamic stall at relatively low Reynolds number. *J. Fluids and Structs.* (2012) **33**:191–209.

[18] Smith, M. J., Jain, R., Grubb, A. and Jacobson, K. Time- and spatially adapting simulations for efficient dynamic stall predictions. *Proc of the 41st Euro. Rotorcraft Forum, CEAS.* (2015) :1–15.

[19] Kaufmann, K., Costes, M., Richez, F., Gardner, A. D. and Le Pape, A. Numerical investigation of three-dimensional static and dynamic stall on a finite wing. *J. American Helicopter Soc.* (2015) **60**:1–12.

[20] Kaufmann, K., Merz, C.B. and Gardner, D.A. Dynamic stall simulation on a pitching finite wing. *J. Aircraft .* (2017) **54**:1303–1316.

[21] Jain, R., Le Pape, A., Grubb, A., Costes, M., Richez, F. and Smith, M. High-resolution computational fluid dynamics predictions for the static and dynamic stall of a finite-span OA209 wing. *J. Fluids and Structs.* (2018) **78**:126–145.

[22] Visbal, M., Yilmaz, T.O. and Rockwell, D. Three-dimensional vortex formation on a heaving low-aspect-ratio wing: Computations and experiments. *J. Fluids and Structs.* (2013) **38**:58–76.

[23] Caleb J.B, Visbal, M.R. and Gordnier, R.E. High-fidelity simulations of a flexible heaving finite-aspect-ratio wing. *AIAA paper.* (2013) :2013–3179.

[24] Pẽrez-Torrõ, R. and Kim, J.W. A large-eddy simulation on a deep-stalled aerofoil with a wavy leading edge. *J Fluid Mech.* (2017) **813**:23-52.

[25] Serson, D., Meneghini, J.R. and Sherwin, S.J. Direct numerical simulations of the flow around wings with spanwise waviness. *J Fluid Mech.* (2017) **826**:714-731.

[26] Brocklehurst, A. and Duque, E. Experimental and numerical study of the British experimental rotor programme blade. *Flight Sim. Tech. Conf. and Exhibit.* (1990) :3008.

[27] Horton, H.P. Laminar separation bubbles in two and three-dimensional incompressible flows. *PhD thesis.* Queen Mary College, University of London (1968).

[28] Young, A.D. and Horton, H.P. Some results of investigations of separation bubbles. *AGARD CP 4.* (1966) :780-811.

[29] De Tullio, N. and Sandham, N.D. Global stability and transition to turbulence of separation bubbles over swept wings. *J Fluid Mech.* (2017) .

[30] Hosseini, S.M., Hanifi, A. and Hennigson, D.S. Effect of freestream turbulence on roughness-induced crossflow instability. *Procedia IUTAM.* (2015) **14**:303-310.

[31] Kaltenbach, H.J. and Janke, G. Direct numerical simulation of flow separation behind a swept, rearward-facing step at $Re_H = 3000$. *Physics of Fluids.* (2000) **12**:2320.

[32] Hadidoolabi, M. and Ansarian, H. Numerical analysis of the flow pattern and vortex breakdown over a pitching delta wing at supersonic speeds. *J Appl. Mech. and Tech. Phys.* (2017) **58**:392-401.

[33] Inagaki, M., Kondoh, T. and Nagano, Y. A mixed-time-scale SGS model with fixed model-parameters for practical LES. *J. Fluids Eng.* (2005) **127**:1–13.

[34] Kim, Y. and Xie, Z.T. Modelling the effects of freestream turbulence on the dynamic stall of wind turbine blades. *Compt Fluids.* (2016) **129**:53–66.

[35] Jasak, H. Error analysis and estimation for the finite volume method with application to fluid flows. *PhD thesis.* Imperial College of Science, Technology and Medicine (1996).

[36] Chiereghin, N., Gursul, I. and Cleaver, D.J. Unsteady force and flow measurements for plunging finite wing. *AIAA Paper.* (2017) **6**:2017-3127.

[37] Visbal, M.R. and Garmann, D.J. Numerical investigation of spanwise end effects on dynamic stall of a pitching NACA 0012 wing. *AIAA Paper.* (2017) :2017–1481.

[38] Calderon, D., Wang, Z., Gursul, I. and Visbal, M.R. Volumetric measurements and simulations of the vortex structures generated by low aspect ratio plunging wings. *Phys of Fluids.* (2013) **25**.

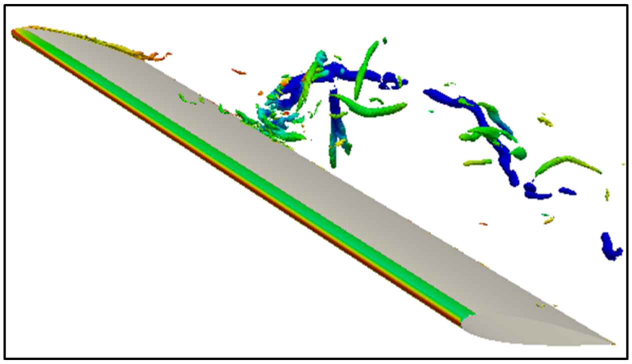

(a) $\phi = 0^\circ$

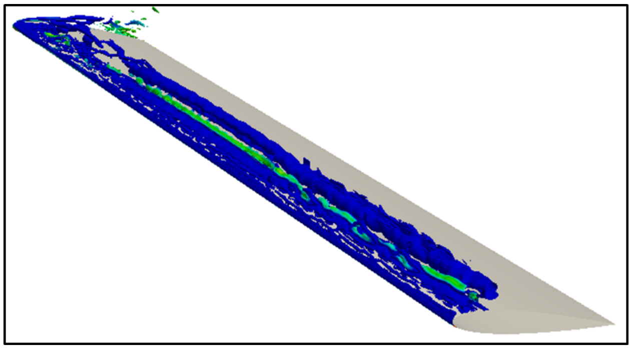

(b) $\phi = 90^\circ$

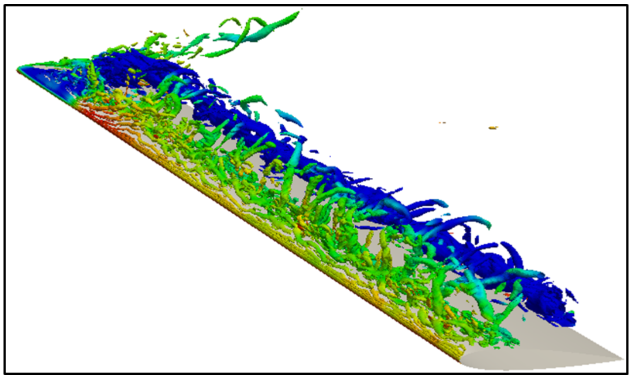

(c) $\phi = 180^\circ$

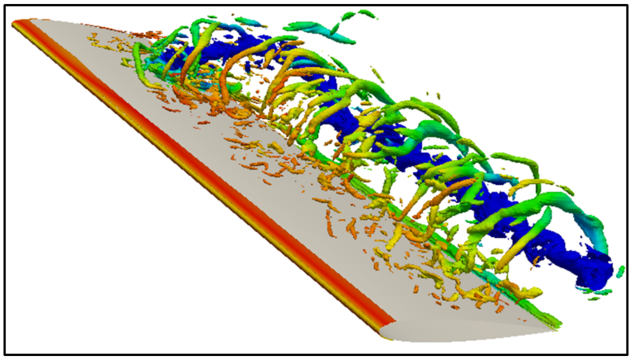

(d) $\phi = 270^\circ$

Figure 12: Iso-surfaces of the second invariant of the velocity gradient tensor (Q=500) at selected phases of the heaving cycle for the un-swept wing, $\Lambda = 0^\circ$, $Re_c = 2 \times 10^4$, $\alpha = 15^\circ$, $k = 0.94$ and $A/c = 0.5$.

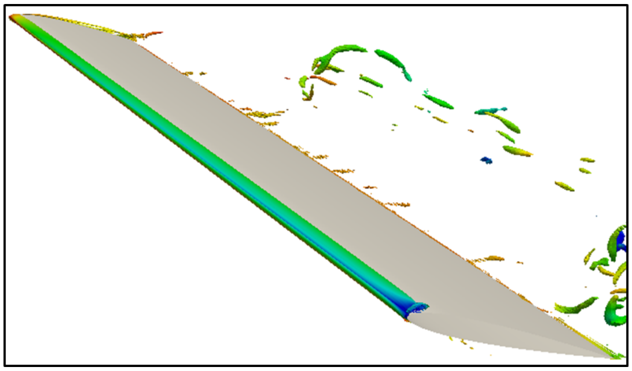

(a) $\phi = 0^\circ$

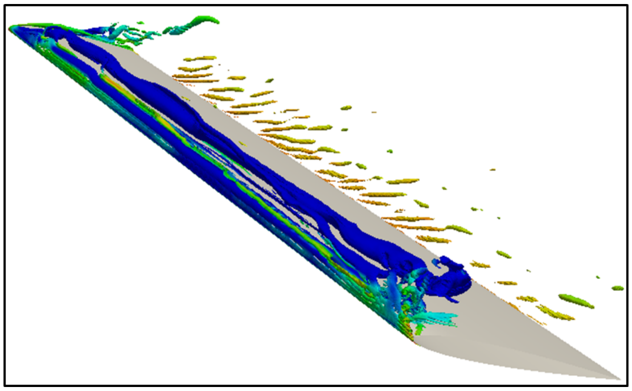

(b) $\phi = 90^\circ$

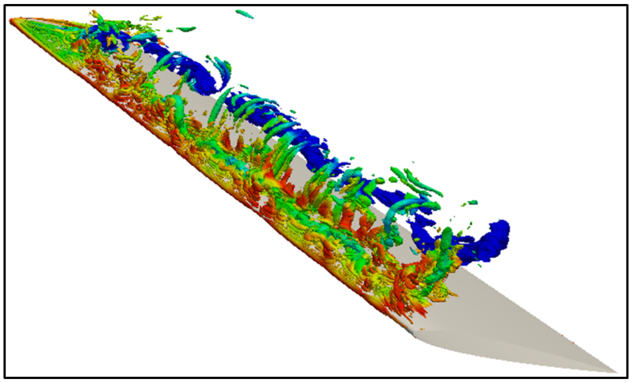

(c) $\phi = 180^\circ$

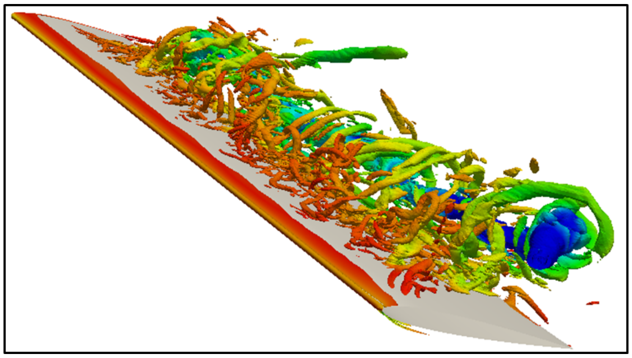

(d) $\phi = 270^\circ$

Figure 13: Iso-surfaces of the second invariant of the velocity gradient tensor (Q=500) at selected phases of the heaving cycle for the swept wing, $\Lambda = 40^\circ$, $Re_c = 2 \times 10^4$, $\alpha = 15^\circ$, $k = 0.94$ and $A/c = 0.5$.

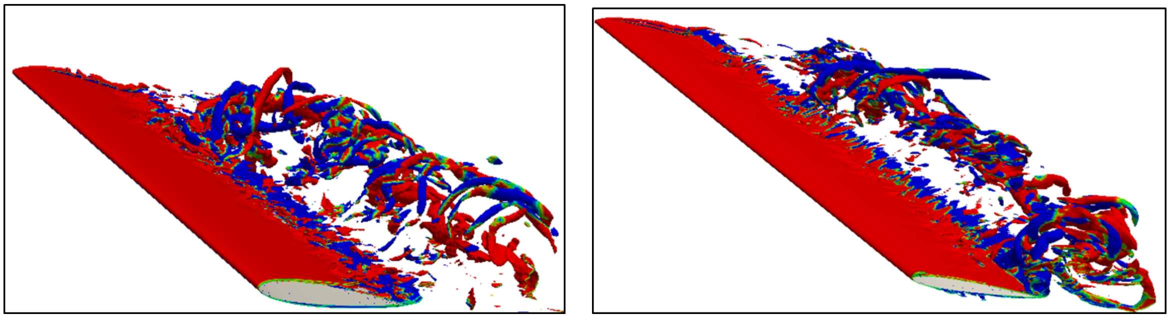

(a) $\Lambda = 0°$, $\phi = 0°$ (b) $\Lambda = 40°$, $\phi = 0°$

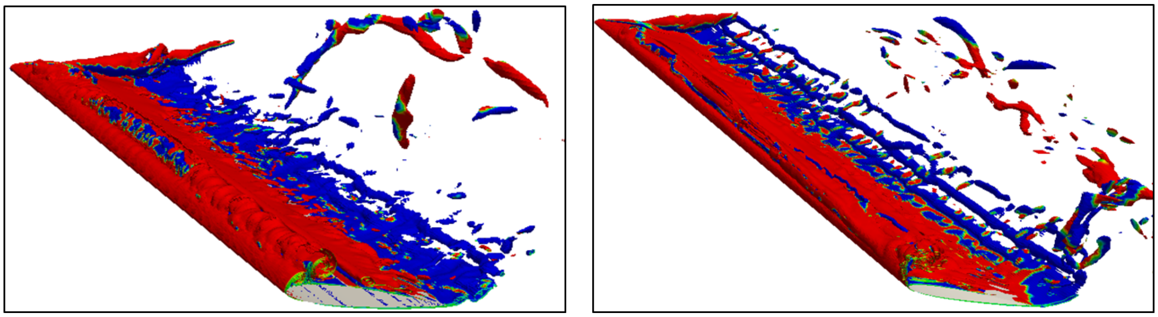

(c) $\Lambda = 0°$, $\phi = 90°$ (d) $\Lambda = 40°$, $\phi = 90°$

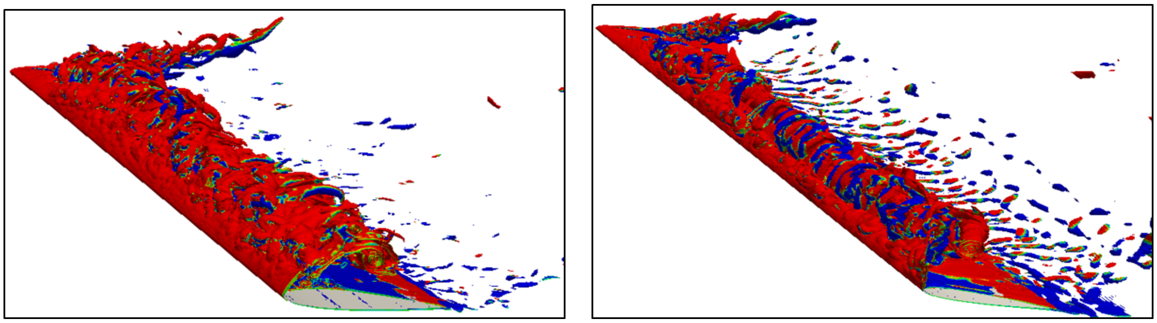

(e) $\Lambda = 0°$, $\phi = 180°$ (f) $\Lambda = 40°$, $\phi = 180°$

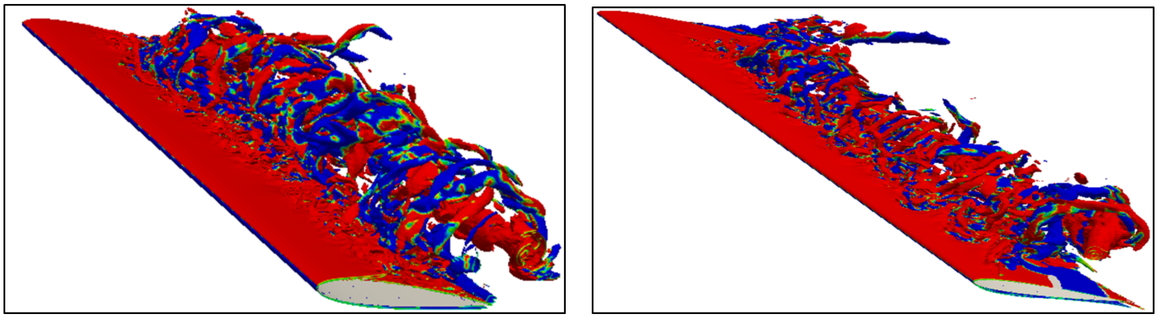

(g) $\Lambda = 0°$, $\phi = 270°$ (h) $\Lambda = 40°$, $\phi = 270°$

Figure 14: Isosurface of instantaneous vorticity for $Re_c = 2 \times 10^4$, $\alpha = 15°$, $k = 0.94$ and $A/c = 0.5$.

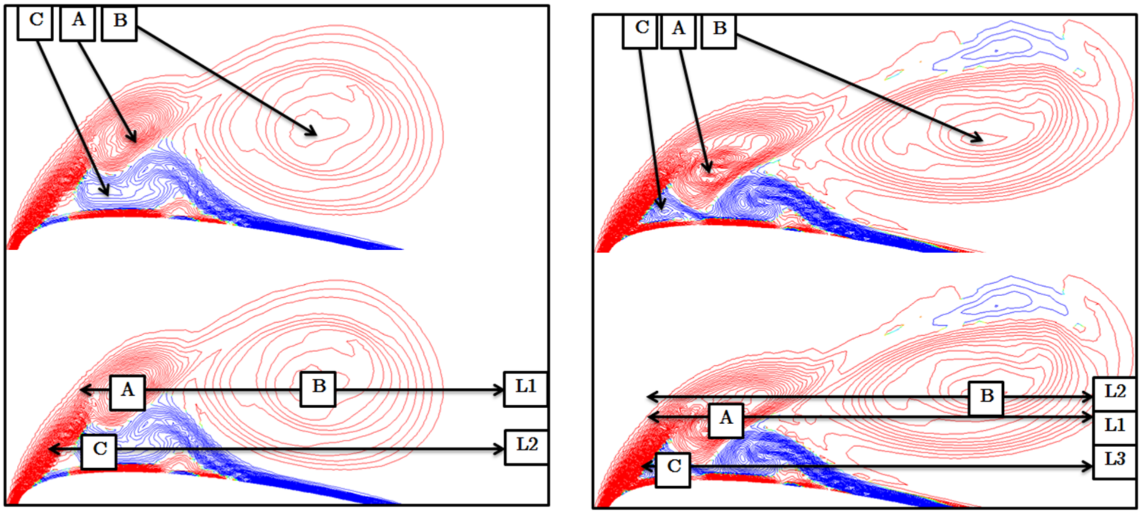

(a) (b)

Figure 15: Contours of w_z over the range of ±30 taken across the centres of vortex cores (top) as well as planes through the cores of A&B (line1, L1), C (line2 ,L2) for the un-swept wing(a-bottom) and through the cores of A (line1, L1), B (line2, L2) and C (line3, L3) for the swept wing (b-bottom), at $\phi = 70°$, $Re_c = 2 \times 10^4$, $\alpha = 5°$, $k = 0.94$ and $A/c = 0.5$.

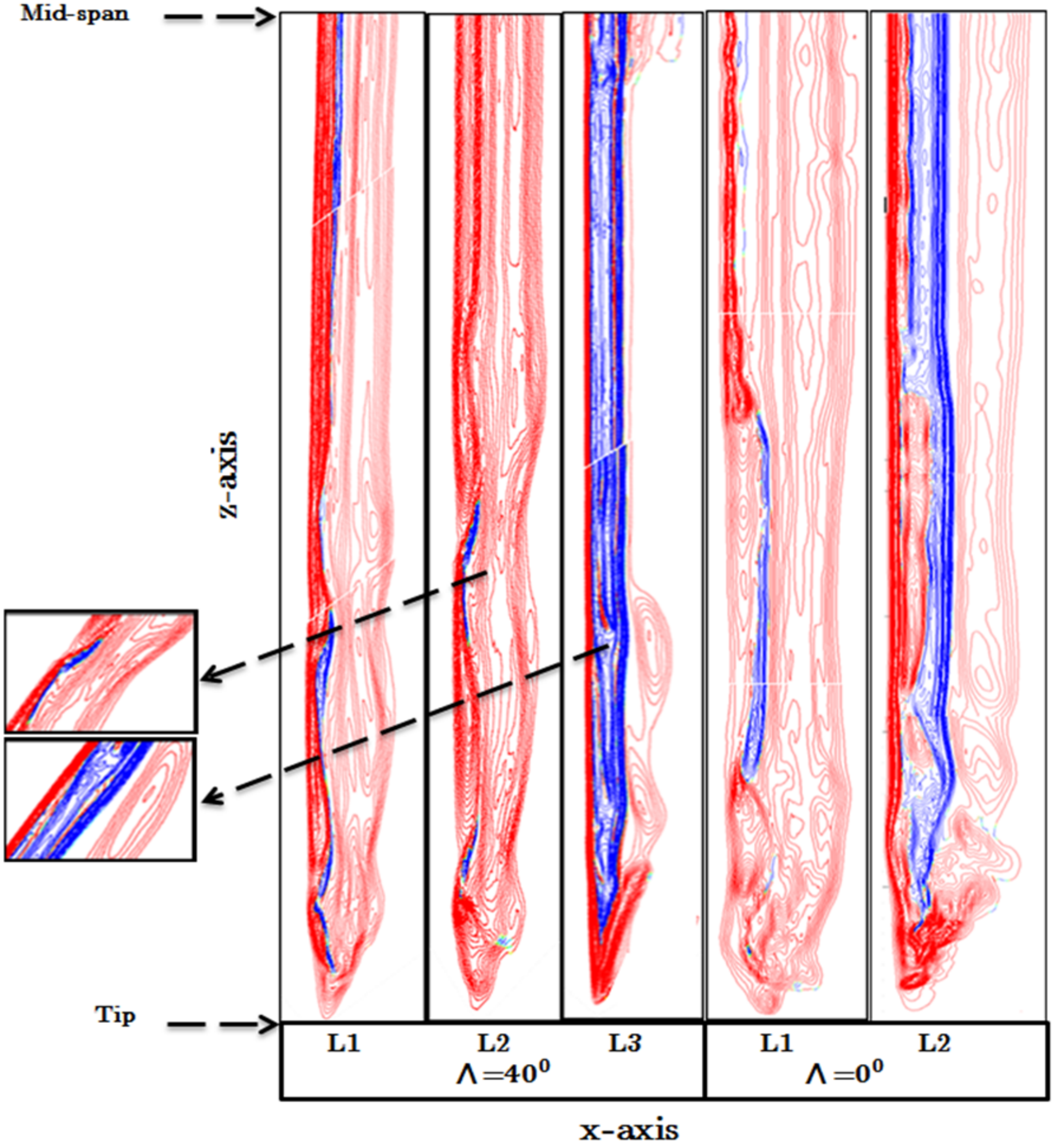

Figure 16: Contours of w_z over the range of ±30, showing the x-z cut plane passing approximately through vortex cores for swept and un-swept wing configuration at $\phi = 70°$, $Re_c = 2 \times 10^4$, $\alpha = 5°$, $k = 0.94$ and $A/c = 0.5$.